SUPPLEMENAL INFORMATION:
Decoupling local mechanics from large-scale structure in modular metamaterials

Nan Yang[1, *] and Jesse L. Silverberg[2, †]

[1] *Tianjin Key Laboratory of the Design and Intelligent Control of Advanced Mechatronical Systems,*
Tianjin University of Technology, Binshuixi Road No. 391, Xiqing District, Tianjin 300384, China
[2] *Wyss Institute for Biologically Inspired Engineering, Harvard University, Boston, MA 02115*

RENDERINGS OF EXAMPLE STRUCTURES

In the main text, we showed snap-shots of a lantern-like kirigami module at various folding configurations as a function of θ for a single set of parameters (Fig. 1*B*). To the best of our knowledge, this structure has not been previously described elsewhere. Therefore, to expand on these illustrations, we calculated and rendered three more examples with different parameters, which provides a broader grasp of how these modules change with θ (Fig. S1).

ADDITIONAL POISSON RATIO DATA

In the main text, we provided data on the Poisson ratios ν_{ZY} and ν_{ZX} for a variety of geometries (Fig. 1*C-F*). While these data illustrated mechanical properties potentially useful for constructing various bulk metamaterials, we include here ν_{YX} for completeness (Fig. S2).

As discussed in the main text, the kirigami module supports two simultaneously negative Poisson ratios (Fig. 1 *C-F*). To further show how the geometric design parameters influence the Poisson ratios, we calculated domains where ν_{ZX} and ν_{ZY} were less than zero and plotted them in the (θ, γ) plane for various α (Fig. S3). We find the design space exhibits non-trivial complexity and offers a wide range of options for specific metamaterial properties. In particular, $\nu_{ZY} < 0$ for all $\theta > 180^\circ$ and any γ. Conversely, the sign of ν_{ZX} is sensitive to θ, α, and γ.

STABILITY OF THE LANTERN-LIKE KIRIGAMI MODULE

In the main text we provided data on the energetic landscape of a single lantern-like kirigami module. Here, we show additional energy plots as a function of θ as the parameters α, γ, θ_0, and k_2/k_1 are varied (Fig. S4 *A-D*). While these data are for idealized models with fully symmetric structure, we note that real materials can be subject to symmetry-breaking heterogeneities. For example, we show with a half-module that 4 distinct stable states are possible (Fig. S4*E*). This finding also applies to the full module, which in turn implies a chain of N voxels in a $1D$ metamaterial supports up to 4^N stable configurations. This high degree of multistability presents an opportunity for engineering non-trivial force-extension relationships with piece-wise smooth behavior, as well as other features not readily achievable with a single module.

MECHANICAL EXPERIMENTS

Kinematic and mechanical designs were prototyped using Mathematica 10.2. This software was used to produce 2D design patterns that were printed and cut from paper sheets (70 g/m^2). Structures were then hand-folded and edges were bonded using cellophane tape. Each structure was then placed inside a closed book and subject to ≈ 10 kg of weight overnight. This process produced structures with an equilibrium configuration angle of $\theta_0 \approx 0^\circ$, and with creased hinges that were generally stiffer than the cellophane-bonded edges. Modules were assembled with $q = 10$ mm, while m and n were chosen as described in the figure captions.

Force-extension measurements on individual voxels and 1D chains (Fig. S5*A-C*) were conducted with a loading speed set to 2 mm/min while the boundaries were mounted with long cellophane strips (Fig. S5*B* and *C*). These loading conditions allowed for ϕ, which quantifies the configuration of the module in the regions closest to the testing apparatus, to smoothly vary during the experiments while still maintaining tension. In our idealized mathematical model, we find the upper and lower portions of the lantern-like module always undergo simultaneous bistability transitions. However, the experiments did not undergo the anticipated *simultaneous* transitions (Fig. S5*B* and *C*, insets). Instead, upper and lower portions of the structure underwent *sequential* bistability transitions. For the simplest case of one voxel (Fig. S5*C*, insets), the two photographs illustrate a typical example taken after the lower portion had transitioned between bistable states, but show the upper portion before-and-after bistable transitions. As can be seen, deformations are almost entirely localized to the upper region of bistability while the lower region maintains its configuration. To facilitate comparison with theory, we converted the

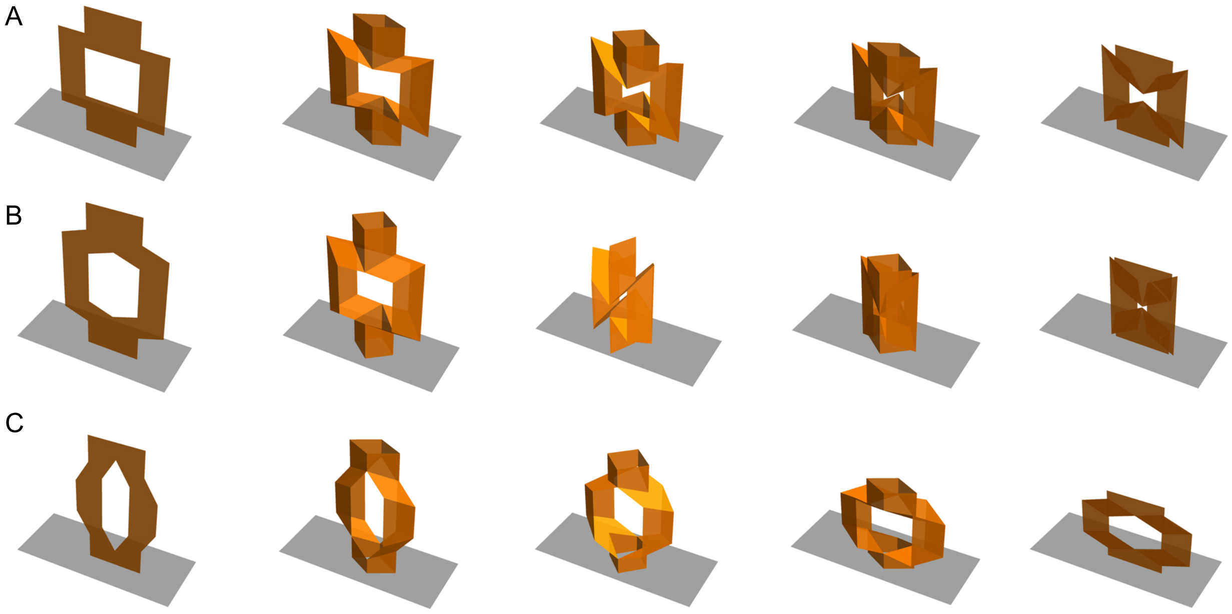

Fig. S1. Example illustrations of lantern-like kirigami module's folding behavior. To elaborate on the main text (Fig. 1B) we show additional example modules at various points in the folding sequence. Geometric parameters are (A) $\alpha = 60^\circ, \gamma = 30^\circ, m/q = n/q = 1$, (B) $\alpha = 60^\circ, \gamma = 50^\circ, m/q = n/q = 1$, and (C) $\alpha = 110^\circ, \gamma = 40^\circ, m/q = n/q = 1$. The columns correspond to $\theta = 0^\circ, 90^\circ, 180^\circ, 270^\circ$, and 360°. Reading left-to-right corresponds to compression along $\hat{z}$, while reading right-to-left corresponds to tension along $\hat{z}$.

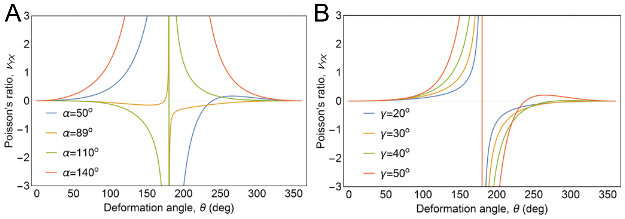

Fig. S2. Poisson ratio ν_{YX}. (A) Poisson ratio for $\gamma = 40^\circ$ and $\alpha = 50^\circ, 89^\circ, 110^\circ$, and 140°. (B) Poisson ratio for $\alpha = 60^\circ$ and $\gamma = 20^\circ, 30^\circ, 40^\circ$, and 50°. Calculations use $m/q = n/q = 1.5$.

measured height $Z(\theta)$ at each moment during testing to the corresponding value of θ that would be anticipated in an idealized case (see equation for $Z(\theta)$ in *Materials and Methods*). This value $\bar{\theta}$ is the *expected deformation angle* in an idealized model, and corresponds to a structure-wide average in the experimental measurements.

To validate the mechanical model for various designs, we fit force-extension measurements to the calculated force-extension relationship $\tilde{F}(\theta) = d\tilde{U}/d(Z/q)$. To obtain robust results, we performed a simultaneous fit to three consecutive force-displacement measurements of each design, minimizing the difference between computed and experimental data. The fits have three free parameters corresponding to the rest angle θ_0 and the two torsional spring constants k_1 and k_2. We found for the $\alpha = 120^\circ$ module (Fig. S5B, red dashed line) $\theta_0 = (9 \pm 2)^\circ, k_1 = (14.7 \pm 0.2) \times 10^{-3}$ N/mm, and k_2 was bounded to the interval $[10^{-8}, 10^{-4}]$ N/mm. Because the 2-voxel (Fig. S5B, blue dashed line) and 3-voxel (Fig. S5B, black dashed line) structures are assembled from modules that have the same geometry as the 1-voxel module, we expect the fits to identify commensurate parameter values. We found for the 2-voxel structure $\theta_0 = (9 \pm 2)^\circ, k_1 = (6.3 \pm 0.1) \times 10^{-3}$ N/mm, and k_2 was bounded to the interval $[10^{-8}, 10^{-4}]$ N/mm. For the 3-voxel structure, $\theta_0 = (9 \pm 2)^\circ, k_1 = (3.5 \pm 0.1) \times 10^{-3}$ N/mm, and k_2 was bounded to the interval $[10^{-8}, 10^{-4}]$ N/mm. Taken together, we see the fits consistently agree on the value for θ_0 and that it is reasonably close to the estimated value of 0°. Moreover, we see $k_2/k_1 \ll 1$, suggesting k_1 dominates the mechanical properties. If the system were a series of Hookean springs in series, we would expect $k^{2-\text{voxel}} = k^{1-\text{voxel}}/2$ and $k^{3-\text{voxel}} = k^{1-\text{voxel}}/3$. Interestingly, we see the 2-voxel value is slightly less than half the 1-voxel case, while the 3-voxel value is about 1/5 the 1-voxel case. Finally, we note that k_2 was not precisely fit, but the bounded values for k_2 compared to the fitted values for k_1 are consistent with expectation that $k_2 \ll k_1$, which was qualitatively observed during sample fabrication.

Our second batch of mechanical experiments com-

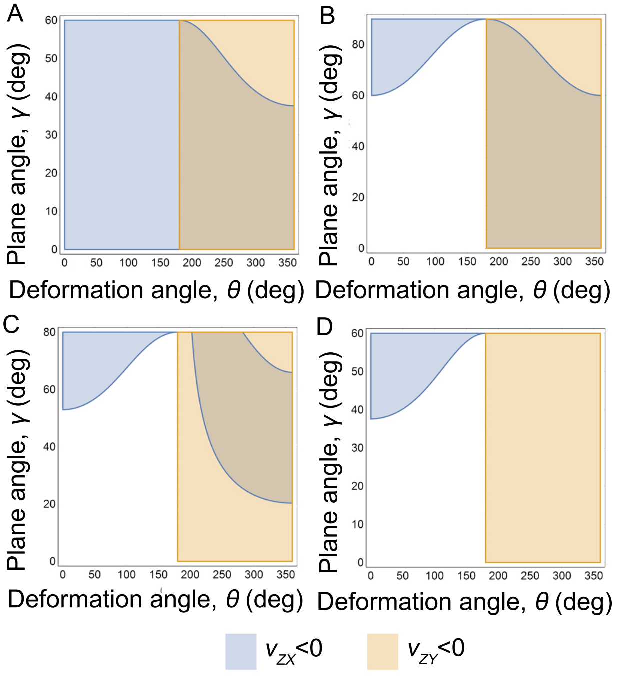

Fig. S3. Regions of negative Poisson ratio. Here, we show domains where $\nu_{ZX} < 0$ (light blue) and $\nu_{ZY} < 0$ (light orange) in the (θ, γ) plane for various values of α. Specifically, (A) $\alpha = 60°$, (B) $\alpha = 90°$, (C) $\alpha = 100°$, and (D) $\alpha = 120°$. Regions of overlapping blue and orange correspond to both Poisson ratios being simultaneously negative, while non-shaded regions correspond to positive Poisson ratios. In all plots, $m/q = n/q = 2$.

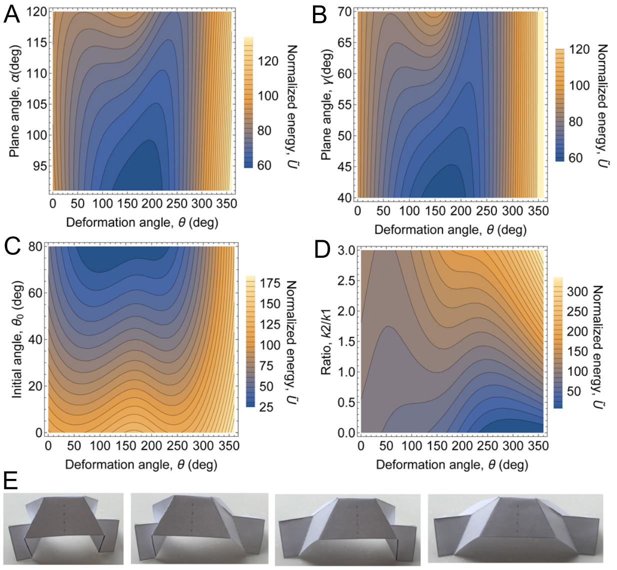

Fig. S4. Stability of the kirigami module. Normalized energy landscapes as a function of θ and various parameters. Specifically, (A) varying α with $\gamma = 60°, m/q = n/q = 1, k_2/k_1 = 1.5$ and $\theta_0 = 10°$. (B) Varying γ with $\alpha = 100°, m/q = n/q = 1, k_2/k_1 = 1.5$, and $\theta_0 = 10°$. (C) Varying θ_0 with $\alpha = 120°, \gamma = 51.2°, m/q = 1.33, n/q = 1.64$, and $k_2/k_1 = 1.5$. (D) Varying k_2/k_1 with $\alpha = 120°, \gamma = 51.2°, m/q = 1.33, n/q = 1.64$, and $\theta_0 = 10°$. (E) A half-module is used to show four distinct stable states accessible under no external loads.

pared the predicted force-displacement relationships for the three geometries. The first sample (Fig. S5*C*, red data) is the same as the 1-voxel sample from the previous measurements (Fig. S5*B*, red data). For the $\alpha = 110°$ module (Fig. S5*C*, orange dashed line), θ_0 was bounded to the interval $[0.01°, 3°]$, $k_1 = (18.4 \pm 0.4) \times 10^{-3}$ N/mm, and k_2 was bounded to the interval $[10^{-7}, 10^{-4}]$ N/mm. For the $\alpha = 100°$ module (Fig. S5*C*, gray dashed line), θ_0 was bounded to the interval $[(10^{-3})°, 11°]$, $k_1 = (19 \pm 2) \times 10^{-3}$ N/mm, and k_2 was bounded to the interval $[10^{-7}, 10^{-4}]$ N/mm. Broadly, we find the fits are again consistent with qualitative expectations. In all cases, θ_0 is close to the expected value of 0°, and the values for k_1 are self-consistent across all measurements as well as with previous work[1]. While some parameters are poorly bounded by the fits, the "non-stiff" nature of these variables serves to indicate their weakness in determining the overall fit quality relative to the tightly bounded, or "stiff," parameters.

We also note that all experiments were conducted under tension in order to avoid the complex non-linear buckling instabilities often found in compression. For example, a failure mode leading to out-of-plane deformations is analogous to Euler buckling found in compressed rods[2]. Additionally, localized bistability transitions or "collapses" can also lead to broken symmetry, as has been observed in origami-inspired bellows[3].

To supplement the experimental force measurements described above (Fig. S5 *B* and *C*), we also show the same data presented as a function of displacement along the $\hat{z}$-axis (Fig. S6), which may be a more intuitive functional form for certain applications. Notably, this presentation of the measurements does not utilize a back-calculated value for θ corresponding to a given height Z. As can be seen, the theoretical model still fits the measured data quite well.

1D AND 2D DESIGN PATTERNS

We show here design patterns for the 1D and 2D metamaterials (Fig. S7). Essentially, the structures are split along the $\hat{x}\hat{z}$ mid-plane and "opened" so that their edges are connected. This connected edge becomes the vertical line of left-right symmetry in the middle of the folding diagram.

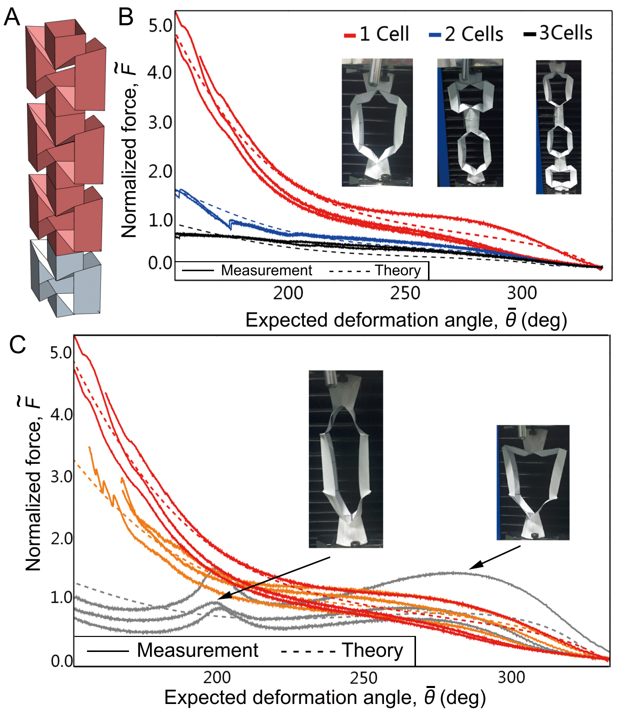

Fig. S5. Assembly of kirigami modules into voxelized 1D mechanical metamaterials. (A) A repeated pattern along the $\hat{z}$-axis of a single voxel (gray) leads to a 1D chain of voxels (gray and pink). (B) Mechanical tests of experimentally fabricated structures (solid lines; geometry based on red voxel in Fig. 2 *A-C*, $\alpha = 120°, \gamma = 51.2°, m/q = 1.33$, and $n/q = 1.64$) show good agreement with theoretical predictions (dashed lines) for 1, 2, and 3 connected voxels. We show three consecutive force-displacement measurements for each structure indicating reproducibility with physical engineering materials. (C) We fabricated and mechanically tested the three gray, orange, and red voxels (Fig. 2 *A-C*) demonstrating each unit has unique mechanical properties. This ability to have geometrically compatible voxels with independently assigned mechanical properties is a key advantage of the $N_p - N_c > 0$ design strategy. Each sample was measured three consecutive times (solid lines) and compared to theory (dashed lines). An empirical phenomenon not predicted by our idealized model are the double-peaks in the $\alpha = 100°$ (gray curves) data. These arise from an asymmetric transition between stable points (Fig. 1 *G-H*) associated with the upper and lower halves of each voxel (inset). In (B) and (C), the expected deformation angle $\bar{\theta}$ is the value of θ calculated from the total measured length of the structure along $\hat{z}$.

LATTICE KIRIGAMI, AUXETIC HONEYCOMBS AND RIGID ROD NETWORK DESIGNS

While various auxetic structures have long been studied for their geometrically-driven properties, lattice based kirigami and honeycomb-like patterns are two areas of contemporary interest for their applications in biomedical devices, graphene-based materials, and as a general mechanical design motif[4–12]. In these designs, a family of mechanical properties including negative Poisson

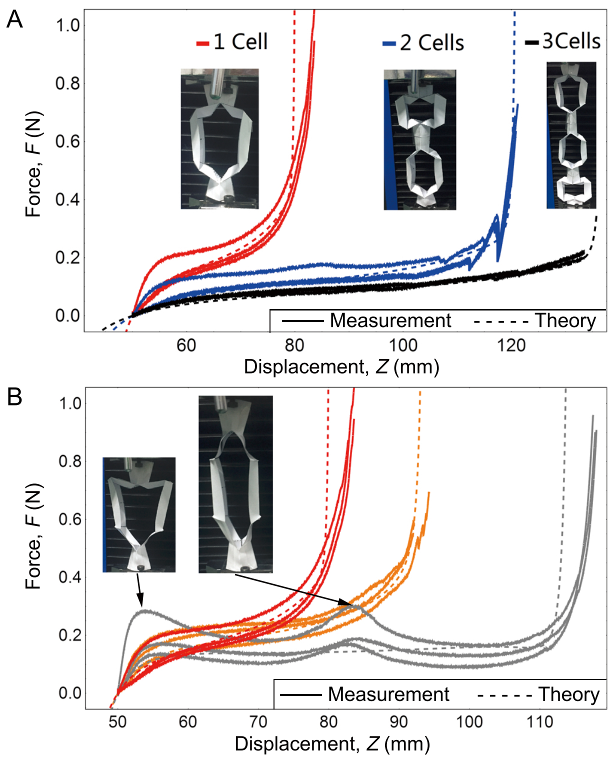

Fig. S6. Experimental measurements presented as a function of voxel height Z. (A) Force-displacement curves for 1, 2, and 3 voxels strung together in a 1D metamaterial. (B) Force-displacement curves for a single voxel with various parameter values. In all plots, solid lines are experimental measurements, dashed lines are fits to theoretical calculations.

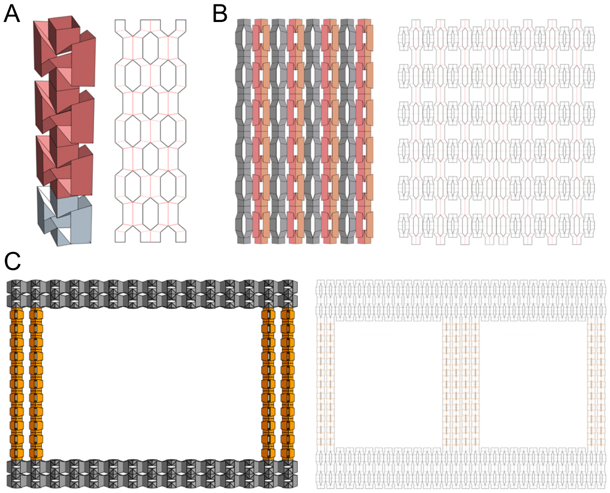

Fig. S7. Metamaterial design patterns. (A) 1D metamaterial design pattern. 2D metamaterial design pattern for the (B) zero bulk Poisson ratio and (C) mechanical cloak structure.

ratio and tunable stiffness has emerged as a generic set of qualities that can be expected from these structures. Nevertheless, when these structures are fabricated, there is a deep coupling of mechanical response between neighboring unit cells that limits the available design space and potential for modularity, especially for 3D structures. A potentially impactful area of research, therefore, would be in developing a modular design strategy similar to the one proposed in the main text specifically for these lattice kirigami and honeycomb-like structures. The benefits over the lantern-like kirigami structure proposed in the main text could include an easier 1-step manufacturing processes as well as rapid deployment in commercially useful materials such as graphene.

Continuing to think about how the ideas proposed in the main text could be realized in practical situations, we turn our attention to network based structures formed from rigid rods (Fig. S8). These lattices have a one-to-one mapping where creases become rods and vertices become joints. Structures similar to the example renderings shown here have been engineered and found to possess a variety of interesting metamaterial properties such as pentamode structure[13, 14] and topologically protected deformations[15, 16]. While such rod-and-stick like structures may be easier to fabricate in practical contexts, it remains unknown whether metamaterial properties can be translated between these two design motifs. In particular, the origami facets typically provide a bending rigidity that resists deformation. For these rod-and-stick structures, the equivalent bending stiffness goes to zero, leading to a different constraint network. Nevertheless, the similarities may still be worth exploring given the opportunities to employ alternative fabrication technologies. A potentially useful analogy from crystallography is the notion of a real space lattice and the corresponding reciprocal lattice in dual space. In the same way solid state physics has established techniques to map frequency-domain phenomena in the dual space to physical properties in real space, there may be a similar connection between the origami-inspired mechanisms and rod-lattice mechanisms. Whether this metaphor offers practical insights would be a subject worth further investigation, since it may lead to a generic method for mapping between two different metamaterial structures with related properties.

POROUS AND BIPHASIC METAMATERIALS

In terms of applications, porous mechanical metamaterials present interesting opportunities for the framework proposed in the main text. For example, many mechanically-responsive biological materials such as cartilage, muscle, lung tissue, and skin are biphasic. That is, they consist of water-saturated solid structures. Along these lines, we can conceive of a biologically-inspired class of biphasic mechanical metamaterials. As an example, we propose that voxelized 3D structures assembled from kirigami modules would form the solid phase, while fluid saturating the structure would form the liquid phase. The structures discussed in the main text are particularly well-suited for these applications since they are highly porous, which would allow fluids to rapidly equilibrate.

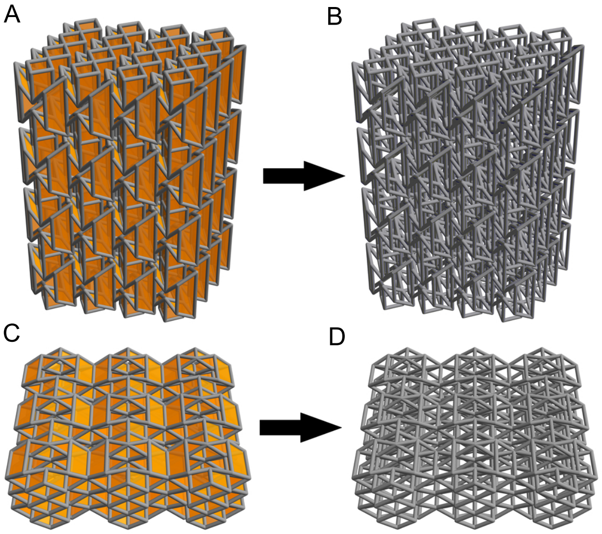

Fig. S8. Rigid rod network materials. Here, we show that a rigid-rod material can be generated by taking (A) the crease pattern of a voxelized kirigami metamaterial, and (B) converting the creases to rods and vertices to joints. A similar mapping (C,D) shows another example structure.

---

[*] yn@tjut.edu.cn
[†] jesse.silverberg@wyss.harvard.edu

[1] Jesse L Silverberg, Arthur A Evans, Lauren McLeod, Ryan C Hayward, Thomas Hull, Christian D Santangelo, and Itai Cohen. Using origami design principles to fold reprogrammable mechanical metamaterials. *Science*, 345(6197):647–650, 2014.

[2] Lev Davidovich Landau, Evgenij M Lifsic, LP Pitaevskii, and AM Kosevich. *Course of Theoretical Physics: Volume 7, Theory of Elasticity.* Pergamon Press, 1986.

[3] Austin Reid, Frederic Lechenault, Sergio Rica, and Mokhtar Adda-Bedia. Geometry and design of origami bellows with tunable response. *Physical Review E*, 95(1):013002, 2017.

[4] Nicholas Karnessis and Gaetano Burriesci. Uniaxial and buckling mechanical response of auxetic cellular tubes. *Smart Materials and Structures*, 22(8):084008, 2013.

[5] Kun Cai, Jing Luo, Yiru Ling, Jing Wan, and Qing-hua Qin. Effects of size and surface on the auxetic behaviour of monolayer graphene kirigami. *Scientific Reports*, 6, 2016.

[6] Robin M Neville, Fabrizio Scarpa, and Alberto Pirrera. Shape morphing kirigami mechanical metamaterials. *Sci-*

entific Reports, 6:31067, 2016.

[7] Terry C Shyu, Pablo F Damasceno, Paul M Dodd, Aaron Lamoureux, Lizhi Xu, Matthew Shlian, Max Shtein, Sharon C Glotzer, and Nicholas A Kotov. A kirigami approach to engineering elasticity in nanocomposites through patterned defects. *Nature Materials*, 14(8):785–789, 2015.

[8] Yigil Cho, Joong-Ho Shin, Avelino Costa, Tae Ann Kim, Valentin Kunin, Ju Li, Su Yeon Lee, Shu Yang, Heung Nam Han, In-Suk Choi, et al. Engineering the shape and structure of materials by fractal cut. *Proceedings of the National Academy of Sciences*, 111(49):17390–17395, 2014.

[9] Ruben Gatt, Luke Mizzi, Joseph I Azzopardi, Keith M Azzopardi, Daphne Attard, Aaron Casha, Joseph Briffa, and Joseph N Grima. Hierarchical auxetic mechanical metamaterials. *Scientific Reports*, 5:8395, 2015.

[10] Toen Castle, Yigil Cho, Xingting Gong, Euiyeon Jung, Daniel M Sussman, Shu Yang, and Randall D Kamien. Making the cut: Lattice kirigami rules. *Physical Review Letters*, 113(24):245502, 2014.

[11] Daniel M Sussman, Yigil Cho, Toen Castle, Xingting Gong, Euiyeon Jung, Shu Yang, and Randall D Kamien. Algorithmic lattice kirigami: A route to pluripotent materials. *Proceedings of the National Academy of Sciences*, 112(24):7449–7453, 2015.

[12] Melina K Blees, Arthur W Barnard, Peter A Rose, Samantha P Roberts, Kathryn L McGill, Pinshane Y Huang, Alexander R Ruyack, Joshua W Kevek, Bryce Kobrin, David A Muller, et al. Graphene kirigami. *Nature*, 524(7564):204–207, 2015.

[13] Muamer Kadic, Tiemo Bückmann, Nicolas Stenger, Michael Thiel, and Martin Wegener. On the practicability of pentamode mechanical metamaterials. *Applied Physics Letters*, 100(19):191901, 2012.

[14] Tiemo Bückmann, Nicolas Stenger, Muamer Kadic, Johannes Kaschke, Andreas Frölich, Tobias Kennerknecht, Christoph Eberl, Michael Thiel, and Martin Wegener. Tailored 3d mechanical metamaterials made by dip-in direct-laser-writing optical lithography. *Advanced Materials*, 24(20):2710–2714, 2012.

[15] Bryan Gin-ge Chen, Bin Liu, Arthur A. Evans, Jayson Paulose, Itai Cohen, Vincenzo Vitelli, and C. D. Santangelo. Topological mechanics of origami and kirigami. *Physical Review Letters*, 116:135501, Mar 2016.

[16] CL Kane and TC Lubensky. Topological boundary modes in isostatic lattices. *Nature Physics*, 10(1):39–45, 2014.